Sustainable Energy & Fuels

ROYAL SOCIETY OF CHEMISTRY

PAPER

View Article Online
View Journal | View Issue

Cite this: *Sustainable Energy Fuels*, 2022, **6**, 4866

Efficient direct lignin fuel cells enabled by hierarchical nickel–iron phosphide nanosheets as an anode catalyst†

Fei Liu,‡[a] A. Lusi,‡[b] Harish Radhakrishnan,[b] Hengzhou Liu,[c] Wenzhen Li,[c] Hantang Qin,[d] Shan Jiang,[a] Xianglan Bai[b] and Hu Shan*[b]

Lignin fuel cells are an emerging technology to sustainably produce electricity from renewable natural resources. A high-performance anode catalyst is highly desirable to enhance the power density of lignin fuel cells for practical applications. Here we demonstrated hierarchical nickel–iron phosphide (NiFeP) nanosheets as a novel anode catalyst for direct lignin fuel cells (DLFCs) at low temperature. NiFeP was grown on nickel foam with its stoichiometry readily controlled in the synthesis. When NiFeP with a Ni/Fe ratio of 1 was used, the fuel cell produced a maximum power density of 24 mW cm^{-2}, over 200 times higher than that of microbial fuel cells or alkaline fuel cells. This performance is comparable to liquid flow fuel cells using liquid catalysts. The P incorporation in NiFeP was found to be essential, whereas P leaching resulted in a significant loss of activity, and re-phosphorization of the used catalyst can recover up to ~80% of the freshly prepared catalyst. In addition, hierarchical nanostructures consisting of 2D nanosheets were also beneficial. The power density of lignin fuel cells could be further improved when the cell was fed with purified lignin with less inorganic ash. Our work provided a new platform of anode catalysts for power generation from biomass.

Received 5th July 2022
Accepted 9th September 2022

DOI: 10.1039/d2se00930g

rsc.li/sustainable-energy

Introduction

Lignin is the second most abundant biopolymer (after cellulose) on Earth and is a complex, random 3-D structured aromatic heteropolymer.[1–4] Over 50 million tons of lignin is annually produced as a by-product from the pulp and paper industry. Lignin has also become increasingly available from emerging cellulosic biorefineries. Despite that lignin is abundantly available at low costs, it is commonly considered as a waste stream and mostly burnt onsite for heat and power. Currently, only less than 2% of the pulp and paper industry-derived lignin is utilized to produce bio-based products, such as binders, resins, and dispersants.[5–8] Due to its aromatic molecular structures and high carbon content, lignin could be an excellent precursor of high-performance carbon materials for energy related applications.[9]

Lignin or lignocellulosic biomass can be used as fuels to generate electricity using fuel cells.[10,11] The fuel cell technology has been considered as an efficient, clean, and low-cost way to produce electricity for many applications.[12–14] The overall lignin-to-electricity efficiency by fuel cells has been proven to be much higher than that of electricity generation by combustion.[15,16] One common group of lignin fuel cells, namely indirect lignin fuel cells, can achieve high power density when operated at high temperature.[17] The technique requires external processing to convert raw lignin to more useable fuels, such as hydrogen, syngas, and biochar.[18,19] A large amount of energy is consumed during the processing, therefore diminishing the economic and environmental benefits. In comparison, direct lignin fuel cells that directly convert lignin to electricity are simpler and more energy efficient. Among all the direct lignin fuel cells, microbial fuel cells (MFCs),[20] alkaline fuel cells (AFCs)[21,22] and liquid flow fuel cells (LFFCs)[23,24] have attracted increasing interest in recent years because they can be operated under mild conditions for many potential applications. MFCs using microorganisms to catalyze the degradation and oxidation of lignin usually produce very low power density (<0.1 mW cm^{-2}) that is far away from that required for practical applications.[25,26] The performance is hindered by the poor ability of microorganisms to attack the complex structure of lignin. AFCs using nickel based electrodes and electron transfer mediators as artificial catalysts instead of microorganisms obtain comparable power density to MFCs.[27] By contrast, LFFCs have been demonstrated to be more

[a]*Department of Materials Science and Engineering, Iowa State University, Ames, IA, 50011, USA*

[b]*Department of Mechanical Engineering, Iowa State University, Ames, IA, 50011, USA. E-mail: shanhu@iastate.edu*

[c]*Department of Chemical and Biological Engineering, Iowa State University, Ames, IA, 50011, USA*

[d]*Department of Industrial and Manufacturing Systems Engineering, Iowa State University, Ames, IA, 50011, USA*

† Electronic supplementary information (ESI) available. See https://doi.org/10.1039/d2se00930g

‡ These authors contributed equally to this work.

competitive and appealing, as their power density has been improved significantly from 0.34 mW cm^{-2} in an early study to 200 mW cm^{-2} recently.[15,16,28,29] Most lignin LFFCs were based on liquid catalysts as electron carriers.[10] The extensive screening of redox couples as electron carriers is responsible for the improvement of the fuel cell performance. However, a pretreatment of lignin with electron carriers followed by filtration of insoluble solids may complicate the fuel cell system for practical applications. The difficulty of separating the catalyst from the solution may increase the cost of fuel cells. In addition, the power density of lignin LFFCs is still lower than that of cells fueled with feedstocks from other biomass and biorenewable resources.[30,31] The high performance of these fuel cells partly resulted from the use of novel solid anode catalysts with extraordinary activity. Solid catalysts are designed for heterogeneous catalysis, offering several advantages such as process simplification, ease of catalyst/product separation, and recovery and recycling of catalysts.[32] Moreover, the state-of-the-art synthesis of solid catalysts has revolutionized many electrochemical systems such as water splitting,[33,34] CO_2 conversion,[35,36] and fuel cells.[37–40] Therefore, direct lignin fuel cells using solid anode catalysts seem to be an alternative design to enhance the power density while keeping the simplicity of the system. However, studies on developing highly active solid catalysts for direct lignin fuel cells remain lacking. This is mainly due to the challenge of C–C bond cleavage and oxidation in lignin fuel cells. Noble metal based electrocatalysts have shown some promise in electrocatalytic C–C bond cleavage in lignin models.[41] A Pt anode was used in the lignin based fuel cell, giving a power density of 1.4 mW cm^{-2}.[42] Nevertheless, a more active catalyst for lignin fuel cells is still highly desirable. Ni-based catalysts have been proven as one of the most effective catalysts in many thermocatalytic processes for lignin conversion. It is also reported to be active towards many electrochemical oxidation processes involving C–C bond cleavage and oxidation, such as methanol oxidation,[43] lignin oxidation,[44] and lignin electro-oxidative depolymerization.[45] However, the effectiveness of Ni-based catalysts in lignin fuel cells remains unexplored.

Herein, we reported a new design of direct lignin fuel cells catalyzed by hierarchical nickel–iron phosphide (NiFeP) nanosheets (Fig. S1†). Our previous studies have demonstrated NiFeP as a highly efficient and multifunctional catalyst for water electrolysis and organic decomposition.[46–48] In this study, hierarchical NiFeP nanosheets with tunable stoichiometry were used as a solid anode catalysts in a lignin fuel cell. The synthesis involved a hydrothermal process to grow NiFe layered double hydroxide (NiFe-LDH) nanosheets on nickel foam and subsequent thermal annealing to convert NiFe-LDH to NiFeP. Interestingly, hierarchical NiFeP nanosheets exhibited high activity towards anodic oxidation of lignin in a direct lignin fuel cell. The cell was fed with raw lignin dissolved in an alkaline solution for the anode and $FeCl_3$ for the cathode, respectively. As a result, NiFeP with a Ni/Fe ratio of 1 possessed the highest performance, giving the fuel cell a maximum power density of 24 mW cm^{-2}, over 200 times higher than that of MFCs or AFCs. The performance of our direct lignin fuel cell is also comparable to many LFFCs using liquid catalysts. It was revealed that the high activity of the solid catalyst originated from P-incorporated transition metal phosphide as well as the hierarchical nanostructure built by 2D nanosheets. In addition, we studied the mechanism for deactivation. The P leaching from the catalyst resulted in a phase transformation from metal phosphide to oxide or hydroxide with a substantial loss of catalytic activity. The activity could be largely restored by regeneration of phosphide under thermal treatment. Furthermore, acid washed lignin with less inorganic contaminants appeared to be a better feedstock to enhance the performance of the fuel cell. Our work established a new platform of catalysts for direct lignin fuel cells, which may open up more opportunities in the development of novel solid catalysts for power generation from lignin.

Results and discussion

Organosolv corn stover lignin provided by Archer Daniels Midland (ADM lignin) and Softwood Kraft Indulin lignin provided by Ingevity (SKL lignin) were used in this work. The results of ultimate and proximate analyses and the molecular weight distributions of the two types of lignin are summarized in Table S1.† ADM lignin had higher averaged molecular weights and polydispersity than SKL lignin. It also had higher oxygen content compared to SKL lignin. Ash content was higher in ADM lignin, which is mainly attributed to its biomass origin. Based on the thermogravimetric analysis (TGA) results shown in Fig. S2,† SKL lignin is thermally much more stable than ADM lignin. In the Fourier transform infrared spectroscopy (FTIR) spectra (Fig. S3†), hydroxyl and carbonyl groups were present more abundantly in ADM lignin than SKL lignin.

As shown in Fig. 1, the catalyst was prepared by growing NiFe-LDH nanosheets on nickel foam, followed by phosphorization to convert NiFe-LDH into NiFeP.

Fig. 2 shows the structural characterization of NiFeP on nickel foam, including the X-ray diffraction (XRD) pattern, scanning electron microscope (SEM) images, transmission electron microscope (TEM) images, high resolution TEM (HRTEM) images, high-angle annular dark-field scanning transmission electron microscope (HAADF-STEM) image and corresponding energy-dispersive X-ray spectroscopy (EDS) elemental mapping, and X-ray photoelectron spectroscopy (XPS) spectra. The XRD pattern (Fig. 2a) shows three major peaks at 44.4°, 51.8°, and 76.3°, corresponding to metallic Ni from the nickel foam substrate. Diffraction peaks at 40.6°,

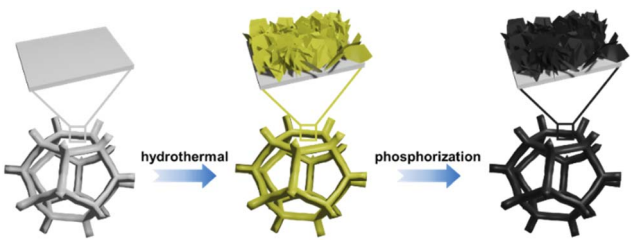

Fig. 1 Schematic illustration of the synthesis of NiFeP on nickel foam.

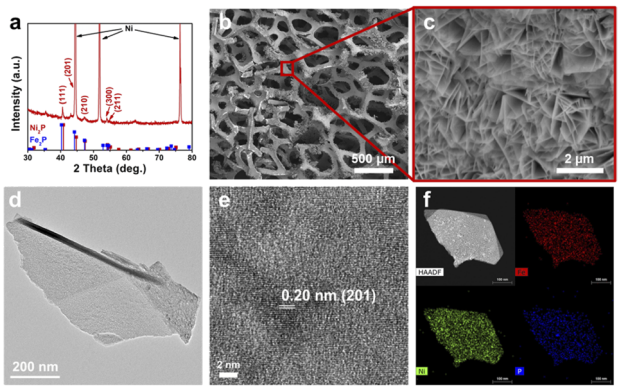

Fig. 2 (a) XRD pattern of NiFeP on nickel foam. (b and c) SEM images of NiFeP on nickel foam. (d and e) TEM and HRTEM images of NiFeP. (f) HAADF-STEM image and the corresponding EDS elemental mapping of Ni, Fe, and P of a NiFeP nanosheet.

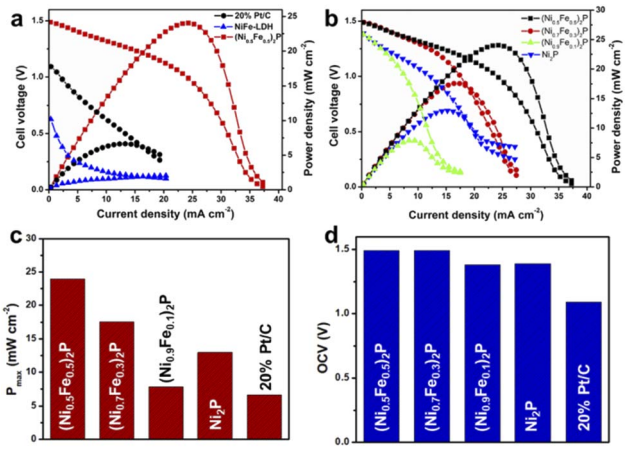

Fig. 3 (a) Polarization and power curves of the fuel cell using different anode catalysts. (b) Polarization and power curves of the fuel cell using NiFeP with different Ni/Fe ratios as the anode catalyst. (c) P_{max} and (d) OCV of the fuel cell using different anode catalysts.

44.4°, 47.3°, 54.1°, and 54.9° are indexed to the (111), (201), (210), (300), and (211) planes of Ni_2P or Fe_2P, respectively. The (111) peak is located between the peak of Fe_2P and Ni_2P, indicating the formation of a solid solution. Fig. 2b shows the low-magnification SEM image of NiFeP on nickel foam with a characteristic porous structure. A zoomed-view SEM image (Fig. 2c) of a nickel branch shows that the nickel foam is covered with a high density of nanosheets. The nanosheets are enriched with Ni, Fe, and P, suggesting the successful formation of phosphide (Fig. S5†). The TEM image (Fig. 2d) confirms the 2D nature of a single nanosheet. A lattice spacing of 0.20 nm (Fig. 2e) can be indexed to the (201) crystal plane of NiFeP. Fig. 2f displays the HAADF-STEM image and EDS elemental mapping of Ni, Fe, and P of a representative NiFeP nanosheet, indicating the uniform distribution of all elements throughout the whole nanosheet. The atomic force microscopy image indicates that NiFeP has a two-dimensional structure, consistent with the SEM and TEM observations (Fig. S4†). The thickness of nanosheets was measured to be ~10 nm. The XPS survey spectrum (Fig. S6a†) further confirms the coexistence of Ni, Fe, and P elements, in accordance with the above EDS elemental mapping results. The high-resolution P 2p spectrum (Fig. S6b†) reveals the presence of metal–P and P–O bonds, indicating the formation of metal phosphide with surface oxidation possibly due to the exposure to air. Furthermore, the high resolution Fe 2p spectrum (Fig. S7a†) shows a peak at a binding energy of 707.0 eV, which can be ascribed to Fe–P species. The peaks at higher binding energy confirm the presence of Fe–O species, indicating the oxidation of Fe–P on the surface. Ni–P and Ni–O species were also respectively confirmed by the peaks at binding energies of 852.5 eV and 855.0 eV in the Ni 2p spectrum (Fig. S7b†).

A polarization curve and power curve were obtained to evaluate the performance of NiFeP as the anode catalyst for the lignin fuel cell. ADM lignin and $FeCl_3$ were used as the anode and cathode, respectively. As shown in Fig. 3a, NiFe-LDH exhibits very low catalytic activity for lignin fuel cells. However, when NiFe-LDH was converted to NiFeP, the activity was boosted significantly, resulting in a much higher open circuit voltage (OCV) and output power density. This implies that the phosphorization process is necessary to activate the catalyst for lignin fuel cells. The maximum power density (P_{max}, power over the electrode area) of the fuel cell using NiFeP (Ni/Fe ratio of 1) as the anode catalyst was calculated to be about 24 mW cm^{-2}. Commercial Pt/C as a typical noble metal catalyst was also used for comparison. Remarkably, NiFeP outperformed the catalytic performance of Pt/C in both OCV and P_{max}. The OCV was increased from 1.1 V to 1.5 V, while P_{max} was improved by 3.6 times. It was found previously that noble metal catalysts (*e.g.*, Pt, Pd, and Ru) were not able to effectively cleave C–C bonds in organic molecules especially for big organic molecules such as lignin.[49] Therefore, a more active catalyst for lignin oxidation is highly desirable. The significant improvement of power density clearly indicates that NiFeP is a very promising catalyst for lignin fuel cells. In addition, the composition of NiFeP was varied to study the composition effect on the catalytic activity and optimize the performance (Fig. 3b). A series of NiFeP catalysts with Ni/Fe ratios of 10/0, 9/1, 7/3, and 5/5 were tested. The actual Ni/Fe ratios in NiFeP were measured by ICP-OES. As shown in Table S2,† the actual Ni/Fe ratios were close to the feed ratios of Ni/Fe precursors in the synthesis. OCV and P_{max} of the fuel cell using different catalysts were obtained to compare the catalyst performance directly (Fig. 3c and d). All the catalysts gave a similar OCV of 1.4–1.5 V. A higher Fe content seemed to slightly improve the OCV. $(Ni_{0.5}Fe_{0.5})_2P$ presented the highest P_{max}, while $(Ni_{0.9}Fe_{0.1})_2P$ was the least active. It is worth noting that all the NiFeP catalysts outperformed commercial Pt/C in terms of fuel cell OCV and P_{max}, indicating the potential of freestanding transition metal based catalysts in future biomass fuel cell applications. Moreover, the power density of our lignin fuel cell catalyzed by hierarchical NiFeP nanosheets is over 200 times higher than those of traditional MFCs and AFCs and is comparable to that of LFFCs using homogeneous catalysts (Table S3†).

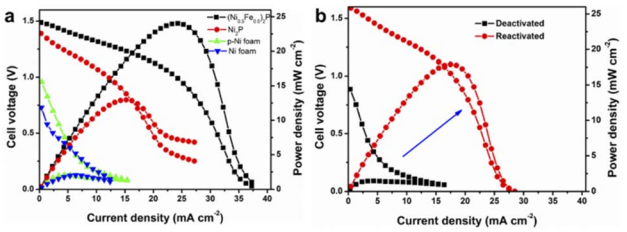

Fig. 4 (a) Polarization curve and the power curve of the fuel cell using different catalysts. (b) Polarization curve and the power curve of the fuel cell with deactivated and activated NiFeP as the catalyst.

The origin of the high catalytic activity of NiFeP was further studied. The comparison between NiFeP and NiFe-LDH implies that the phosphide might be the active phase to dominate the lignin oxidation. Nickel foam presented much lower activity (Fig. 4a). Even phosphorized nickel foam (p-Ni foam) by the same phosphorization process did not show any performance improvement (Fig. 4a). In contrast, Ni_2P on nickel foam exhibited remarkably better performance, though still lower than the Fe-incorporated Ni_2P catalysts (Fig. 4a). This indicates that 2D nanostructures with a high surface area formed by the hydrothermal growth are beneficial. Replacing nickel foam by carbon cloth as the substrate still gave a comparable catalytic performance (Fig. S8†). Furthermore, the porous structure of NiFeP nanosheets could also offer a large number of active sites for electrochemical reactions (Fig. S9†). Therefore, it can be concluded that the high activity of the synthesized catalyst is mainly ascribed to the array of NiFeP nanosheets on the nickel foam.

As the fuel cell reaction proceeded, the catalyst was deactivated. This resulted in a decrease in fuel cell performance, as reflected by a drastic drop in OCV and P_{max} (Fig. S12†). When $(Ni_{0.5}Fe_{0.5})_2P$ was used as the catalyst, the OCV dropped from 1.49 V initially to 0.89 V in 15 min. Similarly, P_{max} decreased by more than 90%. In addition, a constant voltage discharging at an output voltage of 0.2 V was evaluated, and the current density was recorded as shown in Fig. S13†. The current density decreased from 12.3 mA cm^{-2} to 2.4 mA cm^{-2} within 115 min, indicating the deactivation of the catalyst. The SEM image of the catalyst after the fuel cell process shows that there was no obvious nanosheet delamination, and the 2D nanostructure was maintained (Fig. S10a†). However, the carbon content increased significantly, which could be due to the lignin adsorption or char formation on the surface of the catalyst (Fig. S10b†). TGA/DTG analysis of the used catalyst shows constant mass loss in the temperature range of 400–700 °C that could be assigned to the surface carbon decomposition (Fig. S11†). The surface carbon may deteriorate the catalyst's performance by blocking the active sites. Similar deactivation was found for commercial Pt/C, suggesting that the carbon contamination on the surface of the catalyst was responsible for the long-term performance decrease of the fuel cell (Fig. S12†). It's worth pointing out that the deactivated NiFeP still showed comparable performance to Pt/C, whereas Ni_2P outperformed Pt/C (Fig. S12†). To further understand the deactivation of NiFeP, XRD, EDS and XPS analyses of the used catalyst after running the lignin fuel cell for 15 minutes were conducted. The intensity of the typical peak at 41° for NiFeP in the XRD pattern was reduced after the fuel cell reaction, indicating that NiFeP could be partially converted (Fig. S14†). The new phase is likely amorphous or with a trace amount because no new peaks were detected. In addition, the drastically increased O/P ratio from the EDS results suggested that NiFeP could be oxidized into NiFe oxide or hydroxide, which possessed much less catalytic activity for lignin fuel cells (Fig. S10b†). No P signal was detected by XPS, which further confirmed the surface P leaching and phase transformation (Fig. S15†). Iron and nickel oxidation states in the catalyst after the fuel cell process were characterized by XPS. The Fe 2p and Ni 2p spectra of pristine NiFeP confirmed the presence of Fe–P and Ni–P species. After the fuel cell process, the peak corresponding to Fe–P species disappears, whereas Fe–O species are dominant in the surface of the catalyst (Fig. S7c†). Similarly, Ni–P species also vanished from the catalyst after the fuel cell process, as revealed by the Ni 2p spectra (Fig. S7d†). The deactivated NiFeP could be reactivated by thorough rinsing with water, followed by another round of phosphorization. Most surface carbon was removed from the reactivated catalyst, as examined by TGA/DTG analysis (Fig. S16†). The surface NiFe oxide or hydroxide was also re-phosphorized according to the XRD, SEM and EDS results (Fig. S17†). More importantly, the catalytic activity of NiFeP was recovered, as confirmed by the improved performance of reactivated NiFeP compared to deactivated NiFeP (Fig. 4b). The reactivated catalysts showed comparable activity to fresh ones (Fig. S18†). The slight loss of activity could be ascribed to the incomplete removal of the surface carbon adsorption, which would block the active sites for fuel cell reactions.

Table 1 GPC results of ADM lignin before and after the fuel cell process

Sample	Number average M_n	Weight average M_w
Raw lignin	1174	5284
KOH treated lignin	432	877
Lignin after FC	408	867

The post reaction product after the fuel cell process was first neutralized to remove KOH and further analyzed. No lignin-derived monomers could be detected from the post reaction products, suggesting that there was no significant decomposition of lignin during the fuel cell process with the catalyst. The molecular weight distribution of the post reaction product was also analyzed. Since KOH was used during the full cell process whereas bases can promote lignin decomposition,[50,51] lignin treated with KOH but without the fuel cell process was also analyzed. In Table 1, the molecular weights of the post reaction product were similar to that of the KOH treated lignin, both lower than the molecular weights of the initial raw lignin. Thus, the decreased molecular weight of lignin was due to KOH, rather than the fuel cell process.

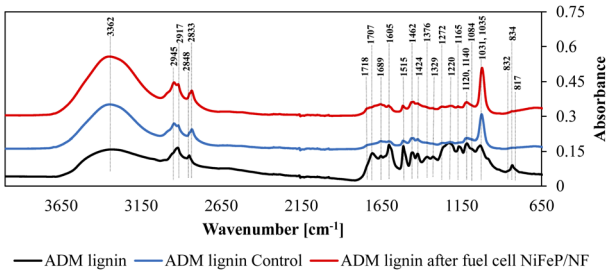

Fig. 5 FTIR spectra of ADM lignin before and after the fuel cell reaction.

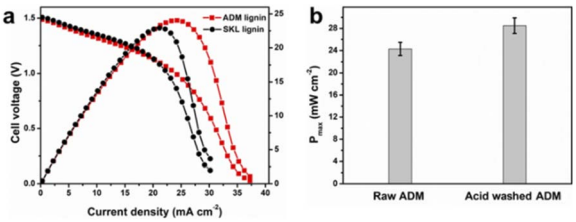

Fig. 6 (a) Fuel cell performance using ADM and SKL lignin as biomass feedstock while other operation conditions are identical. (b) Maximum power density using raw and acid washed lignin as feedstock.

The functional groups of the post reaction products from the fuel cell were also analyzed. In the FTIR results shown in Fig. 5, there is no major difference between the KOH treated lignin and the post reaction product except the band at 1700 cm^{-1} slightly increased for the post reaction product. Since this band is originated from C=O containing functional groups, the partly depolymerized lignin due to the KOH dissolution was further oxidized during the fuel cell process. Functional groups identified by FTIR spectroscopy are summarized in Table S4.†

Despite that there were some variations in their feedstock properties, the fuel cell using SKL lignin shows similar performance compared to AMD lignin (Fig. 6a). Lignin usually contains considerable amounts of inorganic impurities, which originate from both intrinsic biomass and the extraction process. These ash impurities in the lignin may contaminate the catalyst and deteriorate its activity. Thus, ADM lignin was purified to reduce ash content prior to the fuel cell process. Upon dilute acid wash, the ash content in the lignin decreased from 5.9% to 3.0% (Table S5†). The ICP-OES results (Table S6†) indicate that the majority of Ca, K and P in the raw lignin was removed after the washing. The amounts of other elements such as Fe, Mg, and Na were also reduced. The impurities remaining after the acid washing are mostly silicates because they do not dissolve in acidic solutions. Due to the mild purification, there was no noticeable change in the molecular weights of lignin before and after, which is confirmed by GPC (Table S7†). Interestingly, the acid washed ADM lignin produced ~16% higher power density (Fig. 6b), suggesting that the purified lignin would be a better biomass feedstock for fuel cell applications.

Conclusions

In summary, a novel solid catalyst, *i.e.*, hierarchical NiFeP nanosheets, was developed to catalyze direct lignin fuel cells which can convert lignin to electricity. ADM and SKL lignin originating from different biomass species extracted using different chemical methods were tested for the fuel cell. NiFeP nanosheets were grown on nickel foam *via* a hydrothermal process followed by thermal annealing. The stoichiometry of the NiFeP catalyst was carefully tuned, giving the fuel cell a maximum power density of 24 mW cm^{-2} when the Ni/Fe ratio was 1. Our lignin fuel cell catalyzed by hierarchical NiFeP nanosheets greatly outperformed traditional MFCs and AFCs and showed comparable power density to LFFCs using liquid catalysts. The high catalytic activity of NiFeP was attributed to the P-incorporation in phosphide and the hierarchical nanostructure built with 2D nanosheets. The P leaching from NiFeP resulted in the activity loss and decrease in the performance of the fuel cell. An additional phosphorization process was executed to reactivate the catalyst. In addition, purified lignin with less inorganic content was proved to be a better feedstock for fuel cells. Our work will be beneficial for the development of new solid anode catalysts for lignin fuel cells.

Experimental section

Chemicals

Nickel foam (NF, thickness: 1.6 mm, bulk density: 0.45 g cm^{-3}), NH_4F, urea, and $NaH_2PO_2 \cdot H_2O$ were purchased from Sigma-Aldrich. $Ni(NO_3)_2 \cdot 6H_2O$, $Fe(NO_3)_3 \cdot 9H_2O$, and KOH were purchased from Fisher Scientific. Lignins were Archer Daniels Midland Corn Stover Lignin (ADM lignin) and Ingevity Softwood Kraft Indulin AT Lignin (SKL lignin). Milli-Q water with a resistivity >18.0 MΩ cm was used in the preparation of aqueous solutions.

Synthesis of NiFe-LDH and NiFeP

Nickel foam (2 × 5 cm) was first pretreated under sonication in 6 M HCl, ethanol, and water for 15 min, respectively. The cleaned nickel foam was then immersed in the solution containing 4 mmol of NH_4F, 10 mmol urea, 4 mmol total amount of $Ni(NO_3)_2 \cdot 6H_2O$ and $Fe(NO_3)_3 \cdot 9H_2O$, and 40 mL of water. The feed ratio of Ni/Fe was tuned from 10/0, 9/1, and 7/3 to 5/5 to prepare the material with different stoichiometries. The mixture was transferred into a 50 mL Teflon-lined stainless steel autoclave, sealed, and kept at 120 °C for 6 h for hydrothermal growth of NiFe-LDH on the nickel foam. After the hydrothermal process, the nickel foam was separated from the solution, thoroughly rinsed with water under the assistance of mild sonication and dried at 60 °C in air. To convert NiFe-LDH into NiFeP, the as-synthesized NiFe-LDH on nickel foam and 1.0 g of $NaH_2PO_2 \cdot H_2O$ were put in two ceramic boats inside a tube furnace with $NaH_2PO_2 \cdot H_2O$ powder at the upstream of the gas flow. The furnace was heated to 300 °C at a ramping rate of 2 °C min^{-1} and kept at this temperature for 2 h under Ar protection.

Lignin purification

The acid washing process was accomplished by adding 1 g of lignin samples in 30 mL of 0.1 N hydrochloric acid solution under stirring for 4 hours continuously and left to stand overnight. The lignin was then repeatedly rinsed with deionized water, followed by drying in a vacuum oven at 40 °C overnight.

Characterization

X-ray diffraction (XRD) patterns were recorded at room temperature on a Rigaku diffractometer with a Cu Kα radiation source (λ = 1.5406 Å). A JEOL 2100 scanning/transmission electron microscope (STEM) operating at 200 kV was used to acquire bright-field transmission electron microscopy images. Aberration corrected high angle annular dark field scanning transmission electron microscopy (HAADF-STEM) images and energy-dispersive X-ray spectroscopy (EDS) elemental mapping were acquired on a Titan Themis 300 probe corrected TEM with a Super-X EDX detector in the Sensitive Instrument Facility of Ames Lab. Scanning electron microscopy (SEM) images and EDS elemental mapping were acquired on a scanning electron microscope (FEI Quanta 250) with an Oxford X-Max 80 detector. The X-ray photoelectron spectroscopy measurements were performed using a Kratos Amicus/ESCA 3400 spectrometer with Mg Kα 1253.7 eV radiation. Ultimate analysis was performed utilizing an Elementar, vario MICRO cube (Elementar, Hanau, Germany) elemental analyzer, with oxygen determination by difference. A minimum of three trials were performed with standard deviation calculated. Proximate analysis was performed on a Mettler Toledo TGA/DSC system. Gel-permeation chromatographic (GPC) analysis was performed on a Dionex/Thermo Scientific Ultimate 3000 Binary Semipreparative LC System (Sunnyvale, CA) equipped with two Agilent PLgel 3 μm 100 Å 300 × 7.5 mm columns and one Mesopore 300 × 7.5 mm column. Fourier transform infrared spectroscopy (FTIR) analysis of the samples was carried out using a Thermo Scientific Nicolet iS10 equipped with a Smart iTR accessory. Inductively coupled plasma (ICP) was performed on the lignin samples to determine inorganic metal content using an optical emission spectrometer (OES) Optima 8000 (PerkinElmer, Shelton, CT). The actual Ni/Fe ratios in NiFeP catalysts were determined by ICP-OES. The GCMS analysis was conducted on an Agilent 7890B gas chromatograph (GC) equipped with an Agilent 5977A mass spectrometer (MS) and flame ionization detector (FID). Two ZB-1701 capillary columns (60 m × 0.250 mm × 0.250 μm) were used in the GC.

Preparation of the anode

For the anode with Pt/C as the catalyst, 5 cm^2 of carbon cloth was used as the anode substrate. The catalyst ink was prepared by mixing 10 mg of catalyst with 100 μL/400 μL/20 μL of deionized water/isopropanol/5 wt% Nafion solution. The ink was then sonicated for 30 min before drop-casting onto the carbon cloth to achieve a Pt loading of 0.4 mg cm^{-2}. For the anodes with $(Ni_xFe_{1-x})_2P$ (x = 0.5, 0.7, 0.9, 1) and NiFe-LDH as the catalyst, nickel foam was directly used as the anode substrate to grow the desired catalyst. The synthesis of NiFe-LDH and $(Ni_xFe_{1-x})_2P$ is described in the previous section. After the synthesis, the nickel foam was cut into 2 × 2.5 cm and directly used as the anode.

Fuel cell test

A liquid flow fuel cell for a direct lignin fuel cell test was set up. The cell is composed of two graphite bipolar plates as anode and cathode electrodes, respectively. A membrane electrode assembly (MEA) is sandwiched between the two bipolar plates to separate the fuel cell into an anode chamber and a cathode chamber. The MEA with an active area of 5 cm^2 is composed of an anode, a Nafion membrane, and a carbon cloth as the cathode backing layer. The anodes containing different catalysts, including $(Ni_xFe_{1-x})_2P$, NiFe-LDH, and Pt/C, were prepared as described in the previous section. 0.5 M $FeCl_3$ and pre-dissolved lignin in KOH (50 mg mL^{-1} lignin in 1 M KOH) were continuously circulated through the cathode and anode chambers at a flow rate of 20 mL min^{-1} by using a peristaltic pump, respectively. The whole flow cell was heated up to a desired working temperature with two electric heating rods connected to a temperature controller. To evaluate the performance of the fuel cell, the polarization curves were measured by using a potentiostat. The output power density was then calculated from the voltage and current density derived from the polarization curves.

Author contributions

F. L., A. L., and S. H. conceived and designed the experiments. F. L., A. L., H. R., and H. L. performed the experiments. F. L., A. L., and S. H. co-wrote the paper. All the authors discussed the results and commented on the manuscript.

Conflicts of interest

There are no conflicts to declare.

Acknowledgements

This work was supported by the Iowa Economic Development Authority's Iowa Energy Center Grant No. 20-IEC-014. The authors thank Dr Wenyu Huang and Ms Jiaqi Yu for their help with the ICP test.

Notes and references

1 E. Adler, *Wood Sci. Technol.*, 1977, **11**, 169–218.
2 F. N. U. Asina, I. Brzonova, E. Kozliak, A. Kubátová and Y. Ji, *Renewable Sustainable Energy Rev.*, 2017, **77**, 1179–1205.
3 F. G. Calvo-Flores and J. A. Dobado, *ChemSusChem*, 2010, **3**, 1227–1235.
4 D. S. Bajwa, G. Pourhashem, A. H. Ullah and S. G. Bajwa, *Ind. Crops Prod.*, 2019, **139**, 111526.
5 G. W. Huber, S. Iborra and A. Corma, *Chem. Rev.*, 2006, **106**, 4044–4098.

6 J. Zakzeski, P. C. A. Bruijnincx, A. L. Jongerius and B. M. Weckhuysen, *Chem. Rev.*, 2010, **110**, 3552–3599.
7 A. Effendi, H. Gerhauser and A. V. Bridgwater, *Renewable Sustainable Energy Rev.*, 2008, **12**, 2092–2116.
8 H. Lange, S. Decina and C. Crestini, *Eur. Polym. J.*, 2013, **49**, 1151–1173.
9 X. Y. Wu, J. H. Jiang, C. M. Wang, J. Liu, Y. Q. Pu, A. Ragauskas, S. M. Li and B. Yang, *Biofuels, Bioprod. Biorefin.*, 2020, **14**, 650–672.
10 E. Antolini, *ChemSusChem*, 2021, **14**, 189–207.
11 X. Zhao, W. Liu, Y. Deng and J. Y. Zhu, *Renewable Sustainable Energy Rev.*, 2017, **71**, 268–282.
12 G. Palanisamy, H.-Y. Jung, T. Sadhasivam, M. D. Kurkuri, S. C. Kim and S.-H. Roh, *J. Cleaner Prod.*, 2019, **221**, 598–621.
13 R.-A. Felseghi, E. Carcadea, M. S. Raboaca, C. N. TRUFIN and C. Filote, *Energies*, 2019, **12**, 4593.
14 J. M. Moradian, Z. Fang and Y.-C. Yong, *Bioresour. Bioprocess.*, 2021, **8**, 14.
15 Y. A. Chen, H. S. Yang, D. H. Ouyang, T. X. Liu, D. H. Liu and X. B. Zhao, *Appl. Catal., B*, 2020, **265**, 118578.
16 D. Ouyang, F. Wang, J. Hong, D. Gao and X. Zhao, *Appl. Energy*, 2021, **304**, 117927.
17 X. Zhao, W. Liu, Y. Deng and J. Zhu, *Lignocellulosic Biomass-Energized Fuel Cells: Cases of High-Temperature Conversion*, Momentum Press, 2015.
18 J.-Y. Kim, S. Oh and Y.-K. Park, *J. Hazard. Mater.*, 2020, **384**, 121356.
19 S. Rangabhashiyam and P. Balasubramanian, *Ind. Crops Prod.*, 2019, **128**, 405–423.
20 B. E. Logan, B. Hamelers, R. Rozendal, U. Schröder, J. Keller, S. Freguia, P. Aelterman, W. Verstraete and K. Rabaey, *Environ. Sci. Technol.*, 2006, **40**, 5181–5192.
21 T. B. Ferriday and P. H. Middleton, *Int. J. Hydrogen Energy*, 2021, **46**, 18489–18510.
22 X. H. Liu, F. Dong, P. Liu, Z. Li, Y. D. Tong, M. N. Feng, M. Q. Hao, Y. Wang and P. P. Zhang, *Fuel Cells*, 2018, **18**, 219–226.
23 C. W. Anson and S. S. Stahl, *Chem. Rev.*, 2020, **120**, 3749–3786.
24 W. Liu, C. Liu, P. Gogoi and Y. Deng, *Engineering*, 2020, **6**, 1351–1363.
25 X. Wang, Y. Feng, H. Wang, Y. Qu, Y. Yu, N. Ren, N. Li, E. Wang, H. Lee and B. E. Logan, *Environ. Sci. Technol.*, 2009, **43**, 6088–6093.
26 G.-L. Zang, G.-P. Sheng, Z.-H. Tong, X.-W. Liu, S.-X. Teng, W.-W. Li and H.-Q. Yu, *Environ. Sci. Technol.*, 2010, **44**, 2715–2720.
27 S. Li and X. Song, *J. Electroanal. Chem.*, 2018, **810**, 55–61.
28 X. B. Zhao and J. Y. Zhu, *ChemSusChem*, 2016, **9**, 197–207.
29 H. H. Weetal, B. D. Forsyth and W. Hertl, *Biotechnol. Bioeng.*, 1985, **27**, 972–979.
30 J. Qi, L. Xin, Z. Zhang, K. Sun, H. He, F. Wang, D. Chadderdon, Y. Qiu, C. Liang and W. Li, *Green Chem.*, 2013, **15**, 1133–1137.
31 J. Qi, N. Benipal, C. Liang and W. Li, *Appl. Catal., B*, 2016, **199**, 494–503.
32 A. Z. Fadhel, P. Pollet, C. L. Liotta and C. A. Eckert, *Molecules*, 2010, **15**, 8400–8424.
33 J. Jin, J. Yin, H. B. Liu, B. L. Huang, Y. Hu, H. Zhang, M. Z. Sun, Y. Peng, P. X. Xi and C. H. Yan, *Angew. Chem., Int. Ed.*, 2021, **60**, 14117–14123.
34 J. Yin, J. Jin, M. Lu, B. Huang, H. Zhang, Y. Peng, P. Xi and C.-H. Yan, *J. Am. Chem. Soc.*, 2020, **142**, 18378–18386.
35 J. Yin, Z. Yin, J. Jin, M. Sun, B. Huang, H. Lin, Z. Ma, M. Muzzio, M. Shen, C. Yu, H. Zhang, Y. Peng, P. Xi, C.-H. Yan and S. Sun, *J. Am. Chem. Soc.*, 2021, **143**, 15335–15343.
36 G. Lee, Y. C. Li, J.-Y. Kim, T. Peng, D.-H. Nam, A. Sedighian Rasouli, F. Li, M. Luo, A. H. Ip, Y.-C. Joo and E. H. Sargent, *Nat. Energy*, 2021, **6**, 46–53.
37 D. Banham, J.-Y. Choi, T. Kishimoto and S. Ye, *Adv. Mater.*, 2019, **31**, 1804846.
38 Y. Wang, H. Su, Y. He, L. Li, S. Zhu, H. Shen, P. Xie, X. Fu, G. Zhou, C. Feng, D. Zhao, F. Xiao, X. Zhu, Y. Zeng, M. Shao, S. Chen, G. Wu, J. Zeng and C. Wang, *Chem. Rev.*, 2020, **120**, 12217–12314.
39 B. Singh, M. B. Gawande, A. D. Kute, R. S. Varma, P. Fornasiero, P. McNeice, R. V. Jagadeesh, M. Beller and R. Zbořil, *Chem. Rev.*, 2021, **121**, 13620–13697.
40 R. L. Borup, A. Kusoglu, K. C. Neyerlin, R. Mukundan, R. K. Ahluwalia, D. A. Cullen, K. L. More, A. Z. Weber and D. J. Myers, *Curr. Opin. Electrochem.*, 2020, **21**, 192–200.
41 T. Cui, L. Ma, S. Wang, C. Ye, X. Liang, Z. Zhang, G. Meng, L. Zheng, H.-S. Hu, J. Zhang, H. Duan, D. Wang and Y. Li, *J. Am. Chem. Soc.*, 2021, **143**, 9429–9439.
42 R. C. P. Oliveira, M. J. Jeremias, M. M. Mateus and D. M. F. Santos, *Fuel Cells*, 2022, **22**, 39–47.
43 C. Wang, L. Chai, X. Cui, Z. Zhou and S. Liu, *J. Phys. Chem. C*, 2021, **125**, 21443–21452.
44 K. Beliaeva, N. Grimaldos-Osorio, E. Ruiz-López, L. Burel, P. Vernoux and A. Caravaca, *Int. J. Hydrogen Energy*, 2021, **46**, 35752–35764.
45 N. Di Fidio, J. W. Timmermans, C. Antonetti, A. M. Raspolli Galletti, R. J. A. Gosselink, R. J. M. Bisselink and T. M. Slaghek, *New J. Chem.*, 2021, **45**, 9647–9657.
46 B. Zhang, Y. H. Lui, L. Zhou, X. Tang and S. Hu, *J. Mater. Chem. A*, 2017, **5**, 13329–13335.
47 B. Zhang, Y. H. Lui, A. P. S. Gaur, B. Chen, X. Tang, Z. Qi and S. Hu, *ACS Appl. Mater. Interfaces*, 2018, **10**, 8739–8748.
48 B. Zhang, Y. H. Lui, H. Ni and S. Hu, *Nano Energy*, 2017, **38**, 553–560.
49 C. Liu, Z. Zhang, W. Liu, D. Xu, H. Guo, G. He, X. Li and Y. Deng, *Clean Energy*, 2018, **2**, 20–28.
50 H. Wang, M. Tucker and Y. Ji, *J. Appl. Chem.*, 2013, **2013**, 838645.
51 J. Xu, C. Li, L. Dai, C. Xu, Y. Zhong, F. Yu and C. Si, *ChemSusChem*, 2020, **13**, 4284–4295.

